Rapid Communications

Mapping Dirac fermions in the intrinsic antiferromagnetic topological insulators $(MnBi_2Te_4)(Bi_2Te_3)_n$ $(n = 0, 1)$

Zuowei Liang,[1] Aiyun Luo,[2] Mengzhu Shi,[1] Qiang Zhang,[1] Simin Nie,[3] J. J. Ying,[1] J.-F. He,[1] Tao Wu,[1] Zhijun Wang,[4,5] Gang Xu,[2] Zhenyu Wang,[1,*] and X.-H. Chen[1,†]

[1]*Department of Physics and Chinese Academy of Sciences Key Laboratory of Strongly-Coupled Quantum Matter Physics, University of Science and Technology of China, Hefei, Anhui 230026, China*

[2]*Wuhan National High Magnetic Field Center and School of Physics, Huazhong University of Science and Technology, Wuhan 430074, China*

[3]*Department of Materials Science and Engineering, Stanford University, Stanford, California 94305, USA*

[4]*Beijing National Laboratory for Condensed Matter Physics, and Institute of Physics, Chinese Academy of Sciences, Beijing 100190, China*

[5]*University of Chinese Academy of Sciences, Beijing 100049, China*

(Received 7 January 2020; accepted 28 September 2020; published 19 October 2020)

Nontrivial band topology combined with magnetic order can lead to rich emergent phenomena, including quantized anomalous Hall effect and axion insulator state. Here we use scanning tunneling microscopy to image the surface Dirac fermions of the newly discovered magnetic topological insulators $MnBi_2Te_4$ and $MnBi_4Te_7$. We have determined the energy dispersion and helical spin texture of the surface states through quasiparticle interference patterns far above Dirac energy. Approaching the Dirac point, the native defects in the $MnBi_2Te_4$ septuple layer give rise to resonance states which extend spatially and potentially hinder the detection of a mass gap in the spectra. Our results impose tight constraints on the magnitude of the possible mass gap at the nanoscale and provide key ingredients for a comprehensive understanding of the electronic structure in this class of fascinating materials.

DOI: 10.1103/PhysRevB.102.161115

The interplay between nontrivial band topology and magnetism provides a fertile ground for the realization of exotic quantum phenomena, including the quantum anomalous Hall effect, axion insulator states, and chiral Majorana modes [1–6]. To achieve these states, one key step is to open a mass gap on the initial massless Dirac spectrum protected by the time-reversal symmetry [7–11]. Currently, the prevalent approach to open this gap is either by magnetic doping [7,8] or through proximity-heterostructure engineering [9], where the material choice and property optimizations are extremely challenging. As of yet, only few examples of the aforementioned phenomena have been experimentally achieved [3,4], let alone ready for practical applications. Therefore an alternate arena for building magnetic topological materials is highly desired.

Recently, several numbers of $MnBi_2Te_4(Bi_2Te_3)_n$ compound series have been proposed as promising magnetic topological insulators with intrinsic A-type antiferromagnetic order [12–22]. The magnetic moments, ferromagnetically ordered in a Mn sub-plane aligning with the c axis [16], are predicted to break the time-reversal symmetry (Θ) and thus open a sizeable mass gap on the (0001) cleaving surface. Soon after their discovery, quantized anomalous Hall conductivity [23] and quantum phase transitions from an axion insulator to Chern insulator [24] have been observed in odd and even layers of $MnBi_2Te_4$, respectively. However, the detailed band structure of the topological surface states remains unclear, and photoemission data show controversial results. Unexpected gapless surface states have been recently reported by high-resolution angle-resolved photoelectron spectroscopy (ARPES) [25–29], in striking contrast with the large gap found in previous measurements [30,31]. Recalling the fact that local perturbations, such as defects and chemical disorders, can give rise to localized resonances and nanoscale fluctuations of the topological surface states [32–35], it is thus critical to study Dirac electrons with a local probe, especially in an energy range near the Dirac point.

Spectroscopic imaging scanning tunneling microscopy (SI-STM) offers a powerful tool to study the scattering properties and spatial inhomogeneity of the surface Dirac electrons. In this work we use SI-STM to directly image the electronic properties of the topological surface states in $MnBi_2Te_4$ (Mn124) and $MnBi_4Te_7$ (Mn147). The quasiparticle interference patterns show clear evidence for the absence of backscattering revealing the spin-momentum locking of the surface states. We find electronic inhomogeneity induced by defects that dominate in the $MnBi_2Te_4$ septuple layers (MBT SLs) but are absent in the Bi_2Te_3 quintuple layers (QLs). These defects induce resonance states near the Dirac energy within a length scale larger than a few nanometers, which potentially impede the detection of a gap in the tunneling spectra.

Single crystals of Mn124 and Mn147 were grown via a solid-state reaction method as described in earlier studies [13,36]. X-ray diffraction measurements were carried out on

*Author to whom correspondence should be addressed: zywang2@ustc.edu.cn

†chenxh@ustc.edu.cn

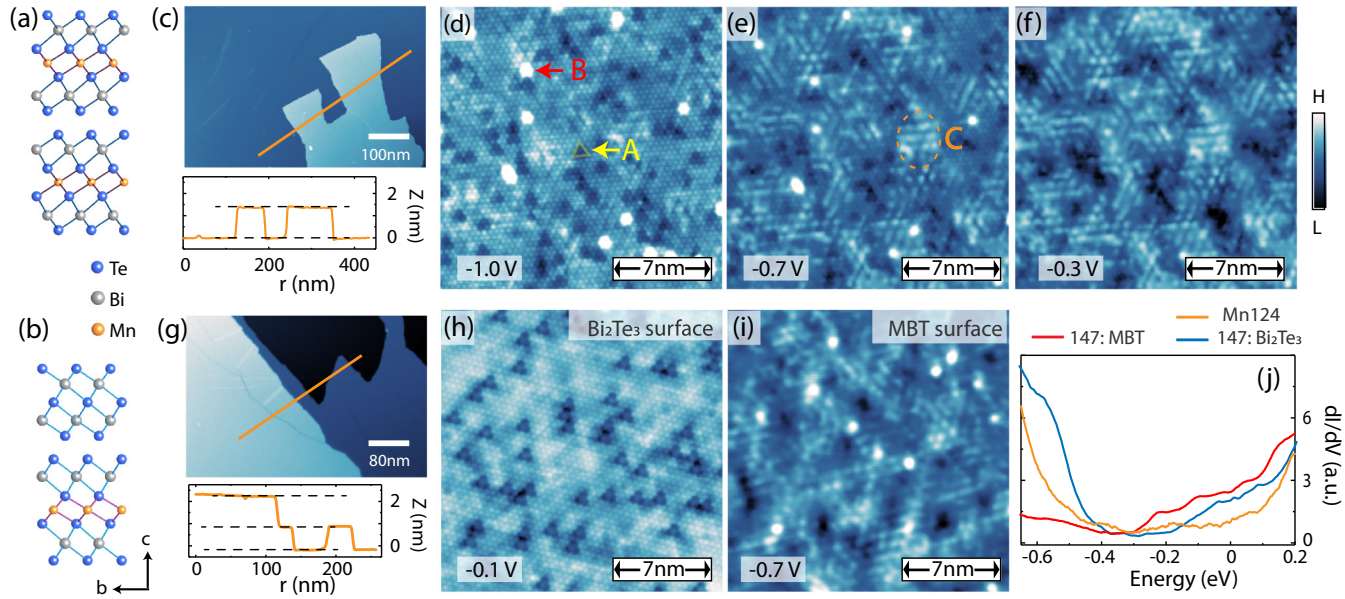

FIG. 1. Surface conditions of Mn124 and Mn147. (a), (b) Schematic of the crystal structures of Mn124 and 147. (c), (g) Large area topographic images of Mn124 and Mn147 showing step edges. The step heights for MBT septuple layer and Bi_2Te_3 quintuple layer are 1.36 and 1.01 nm, respectively. (d)–(f) Atomic-resolution topographic images obtained at different bias voltages in Mn124. Three different types of defects have been found, including the Mn_{Bi} antisite defects (type A), Bi replacing Te atoms on the top surface (type B), and defects in the Mn atomic layer (type C). (h), (i) Atomic-resolution topographic images obtained on different surfaces of Mn147. (j) Tunneling spectra taken on the three types of surfaces.

each sample to confirm its correct phase and high crystalline quality (see Supplemental Material (SM), note 1 [37]). The single crystals were cleaved at room temperature in a vacuum better than 2×10^{-10} Torr and immediately inserted into the STM head, which remained at 5.5 K. PtIr tips were used and tested on the surface of single-crystal Au(111) before performing the measurements. Spectroscopic data were acquired by the standard lock-in technique at a frequency of 987.5 Hz under modulation voltage ~2–12 mV.

The material which we first focus on, Mn124, is a van der Waals (vdW) material formed by stacking Te-Bi-Te-Mn-Te-Bi-Te SLs [Fig. 1(a)]. The crystals cleave naturally between two adjacent layers, resulting in a Te-terminated surface. The topographic image shows a step-edge with a height of about 13.8 Å, consistent with the height of one SL layer [Fig. 1(c)]. Figures 1(d)–1(f) depict atomically resolved images representing a few typical features. Topography at high bias voltage [−1 V, Fig. 1(d)] clearly shows the hexagonal Te lattice with a periodicity of ~0.43 Å. Within this field of view, dark triangular defects (type A) are observed, corresponding to Mn_{Bi} antisite defects in the Bi layer beneath [34]. The estimated spatial concentration of Mn_{Bi} defects is approximately $0.15\,nm^{-2}$, giving a value of 2.5% Mn/Bi substitution. The bright protrusions (type B) are most likely attributable to the Bi replacing the top-layer Te atoms [38], which are rare on the surface. Upon approaching low energies, however, we find a third type of defect (type C) that dominates the entire surface [Figs. 1(e) and 1(f)]; more bias-dependent topographies can

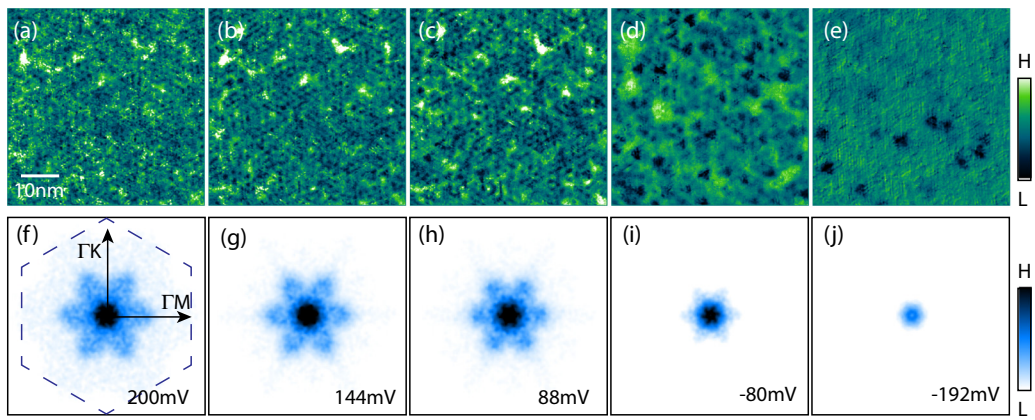

FIG. 2. Quasiparticle interference of Mn124. (a)–(e) Normalized *dI/dV* maps in a 50 × 50 nm field of view at different energies. (f)–(j) Drift-corrected and symmetrized Fourier transforms of the *dI/dV* maps. The dashed hexagon in (f) denotes the surface Brillouin zone.

be found in SM note 2 [37]. A closer look reveals that these features are weakly ordered somewhere, with their positions unchanged at different bias voltages. This indicates that these features are representative of the electronic structure response to strong local perturbations in the crystal that can be imaged at the surface. Unfortunately, these defects overlap with each other due to their large density, making it difficult to identify the chemical species. We have presented the positions and statistics of these three kinds of defects in SM note 3 [37].

To better understand these defects, we have imaged the surface of Mn147, which has Bi_2Te_3 QLs intercalated between the nearest MBT SLs [Fig. 1(b)]. Cleaving could expose two kinds of surfaces—either Bi_2Te_3 or MBT terminations. As shown in Fig. 1(g), these two kinds of surfaces can be identified easily via their respective step heights, which in turn confirms the good quality of our crystals. Again, type-C defects are clearly visible on the MBT SL surface but absent on the Bi_2Te_3-terminated surface, suggesting that these defects are intimately tied to the MBT layers. The concentration of type-C defects estimated by counting, together with other recent reports of nonstoichiometric composition in both Mn124 ($Mn_{0.85}Bi_{2.1}Te_4$, Refs. [16,13]) and Mn147 ($Mn_{0.85}Bi_{4.1}Te_7$, Ref. [21]), suggest that they are most likely to be defects in the Mn layers, i.e., Bi_{Mn} antisite defects or Mn vacancies.

Our next step is to explore the topological surface states. The *dI/dV* spectra, which measure the local density of state (DOS) against energy (in eV), are displayed in Fig. 1(j) for these three kinds of surfaces. The suppression of DOS in the energy ranging from -0.2 to -0.4 eV can be attributed to the bulk gap that embraces the surface states, which will be discussed in greater detail later. Here we note that the spectra taken on the MBT SLs in Mn124 and Mn147 show a distinct line-shape, indicating that the electronic structure is quite sensitive to the stacking layers underneath [29]. To obtain more information on the surface states, we employ Fourier-transform quasiparticle interference imaging (FT-QPI). In FT-QPI, the standing-wave pattern arising from the coherent scattering of quasiparticles can be measured as dI/dV (r, eV) maps and then Fourier transformed to extract the scattering vectors which connect two states on the constant energy contours (CECs). This is a powerful technique to measure the band dispersion and investigate the orbital/spin textures of the electronic states. To remove the set-point effect, we apply the Feenstra technique to normalize the conductance map before the Fourier transform [39,40]. Figures 2(a)–2(e) show the resultant conductance maps at various energies obtained in Mn124, and the standing-wave patterns are visible at high energies. The QPI patterns, as shown in Figs. 2(f)–2(j), exhibit sixfold symmetric peaks along the ΓM direction (more data can be found in SM note 4 [37]).

To understand the origin of these QPI peaks, it is necessary to compare our QPI data with ARPES dispersion and theoretical calculations. It has been well established in Bi_2Te_3 that the hexagonal warped shape of the surface-band CEC dominates the scattering channels far above the Dirac energy [41,42]. For Mn124, the warping effects of the surface state can be illustrated by the anisotropic dispersion along ΓM and ΓK extracted from the laser-APRES data [25,29] and our band calculations with different surface magnetic orders (SM note 5 [37]). As recent ARPES studies have suggested that

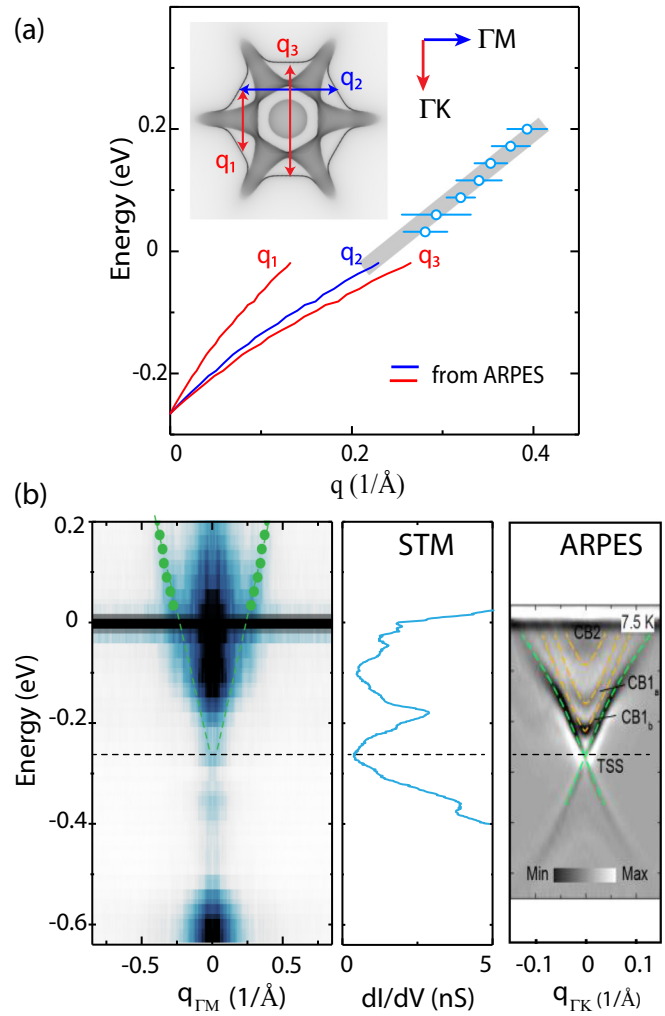

FIG. 3. Identification of the FT-QPI patterns of Mn124. (a) Dispersion of the possible scattering channels calculated from ARPES data [25] and the comparison with QPI data. The inset shows a calculated constant energy contour (CEC) above the Fermi level using a model with paramagnetic order (SM note 5 [37]). The error bars are a sum of the standard deviation width from the Gaussian fit to the peaks and the size of the smoothing window (SM note 4 [37]). (b) Intensity plot of the fast Fourier transform line cut reveals the surface-state dispersion, which matches well with the single dI/dV spectrum and ARPES data [25].

the energy dispersion and Fermi surface topology are most consistent with a model with paramagnetic order, we show a calculated CEC with paramagnetic order at higher energy in the inset of Fig. 3(a) and label the possible q vectors along two high-symmetric directions ΓM and ΓK. Correspondingly, we can extract the dispersion of all possible scattering channels from ARPES data [solid lines in Fig. 3(a)]. A direct comparison with our STM data allows us to identify the QPI peak in our experiment as scattering vector $q_2 = \sqrt{3}k_{\Gamma K}$, a channel allowed by the helical spin texture [Fig. 3(a); see more detail in SM note 4 [37]]. The absence of q_3 along the ΓK direction in our QPI pattern indicates that backscattering is strictly forbidden far above the Dirac energy. To further clarify the momentum-space origin of these peaks, we perform a model

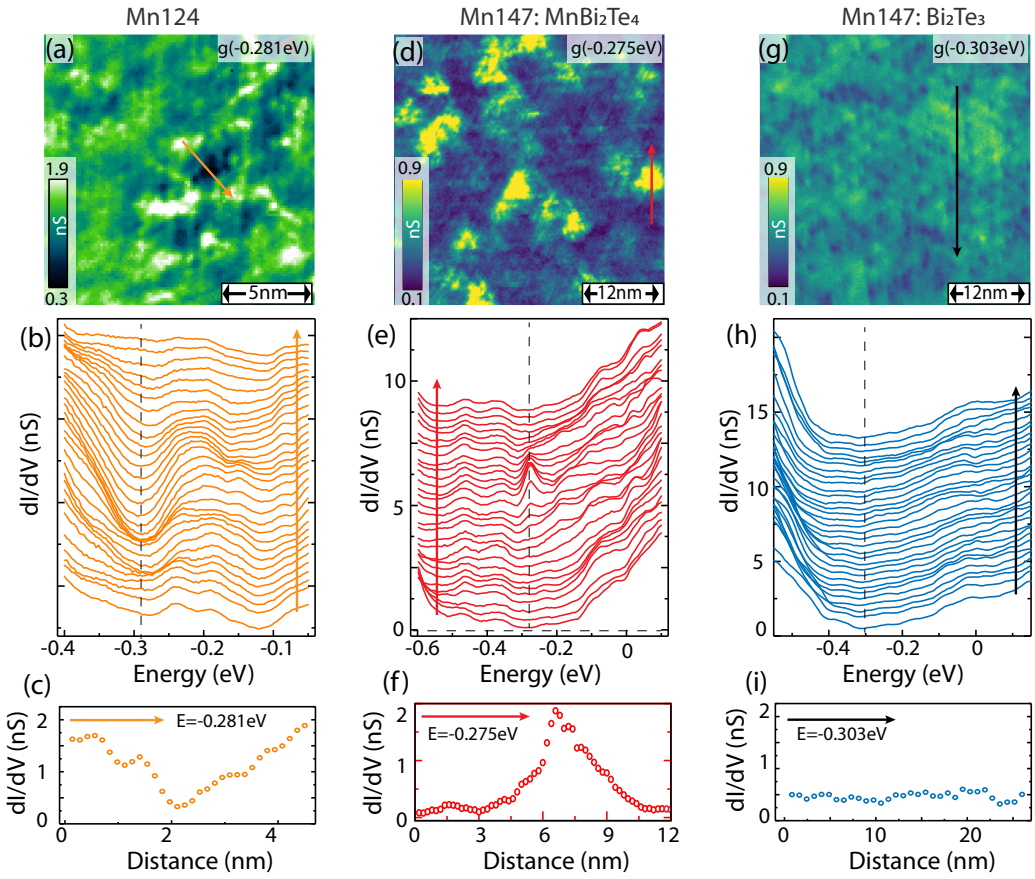

FIG. 4. Electronic inhomogeneity and impurity-induced resonance states near the Dirac energy. (a), (d), (g) Differential conductance maps obtained near the Dirac energy in Mn124 and Mn147. While the local density of state (LDOS) shows pronounced spatial variations on the MBT-terminated surfaces, it is relatively uniform on the Bi_2Te_3-terminated surface. (b), (e), (h) Tunneling spectra taken along lines. Electronic resonance states energetically located close to the Dirac point emerge on the MBT surfaces. (c), (f), (i) Spatial dependent of the resonance state. The spectral weight of the resonance decays over a few nanometers.

calculation of the spin-dependent scattering probability and find good agreement between our STM data and the calculated QPI patterns (see more details in Fig. S6 [37]). At low energy where the dispersion is conic, the helical spin texture also forbids direct backscattering, thus attenuating the total QPI signal [Fig. 2(j)]. The dispersion extracted from both QPI and ARPES data, and the minimum in the DOS, are all consistent with a Dirac point at -280 ± 10 meV (here we ignore the potential mass gap which we will discuss in detail later). We note that the QPI peaks in Mn124 are broader and fuzzier than those obtained in Bi_2Te_3, probably owing to the contribution of the bulk band scattering and the large amount of defects which may reduce the quasiparticle lifetime (Fig. S6 [37]). We have also observed sixfold QPI patterns on both Bi_2Te_3 and MBT surfaces in Mn147 (SM note 6 [37]). Recent ARPES and STM measurements have found Rashba-like splitting bands near the surface of both Mn124 [43] and Mn147 [44], which may also contribute to the total QPI signals.

Having determined the topological nature of the surface state, we now discuss whether a Dirac-mass gap is opened or not by the bulk A-type antiferromagnetic order. As shown in Fig. 3(b), a finite DOS has been clearly observed near the Dirac point in Mn124, in good agreement with the gapless spectrum found by high-resolution ARPES data [25–29]. On the other hand, we do find a large amount of defects (2.5% of type A and about 11% of type C) in the samples. Since these defects could affect the local DOS and generate resonance states near the Dirac energy [35], it is critical to measure the spatial evolution of the DOS. To proceed, we acquire dI/dV (r, eV) spectra on a densely spaced grid in a 15×15 nm area of Mn124. The differential conductance recorded near the Dirac point never reaches zero [Fig. 4(a)], in sharp contrast to the opening of a gap. However, the DOS is quite inhomogeneous and seems to be directly related to the presence of type-C impurities (see SM note 7 [37]). We first examine spatially resolved dI/dV spectra collected along a line [Fig. 4(b)]. The tunneling spectra show pronounced spatial variations: At energies far away from the Dirac point, the spectral line shapes are quite similar, while near the Dirac point electronic resonance states emerge due to the presence of defects. To obtain a visual sense of the variations of the spectra, we sort all the spectra obtained in this area into 20 bins against the dI/dV values at -281 meV and then average all spectra in each bin. The binned spectra, which well capture the inhomogeneity, are shown in SM note 8 [37]. Figure 4(c) maps the spatial distribution of the DOS along the line shown in Fig. 4(a), which passes through the region showing minimum differential conductance in this field of view. The V-shaped bottom of

this curve reveals that the decay length of the resonant state is larger than the average distance between the defects. To obtain a more complete picture of the resonance state, we have measured the dI/dV (r, eV) spectra of both MBT and Bi_2Te_3 surfaces of Mn147. Similar behavior can be found on the MBT-terminated surface, where sharp resonance peaks are clearly observed near the Dirac energy with spectral weight spreading over distances of a few nanometers [Figs. 4(d)–4(f)]. In sharp contrast, the local DOS near Dirac energy is relatively uniform on the Bi_2Te_3 terminations, showing very weak spatial variations [Figs. 4(g)–4(i)]. These observations further suggest that the resonance states are most likely induced by the defects in the Mn atomic layers.

The experimental realization of QAHE in Mn124 [23], which confirms the existence of a gapped Dirac state, and the finite DOS at the Dirac energy have led to an apparent paradox. The possible resolutions proposed so far include different spin reconstructions near the surface [25,27,29], the presence of magnetic domains [25], and weak hybridizations between Dirac fermions and the magnetic order [26]. However, a recent study using magnetic force microscopy has revealed robust A-type antiferromagnetic order on the surface layer of bulk Mn124 [45], and quantized Hall conductance (97%) can be achieved without an external magnetic field [23], further complicating the situation. Our observations provide a natural explanation for the absence of a mass gap in spectroscopic measurements. The extended states (∼5 nm) induced by defects are significantly overlapping in real space and thus create a non-negligible spectral weight over the entire surface. These resonance states are always generated in the vicinity of the Dirac energy, impeding the detection of the mass gap of the mobile Dirac spectrum when the gap is relatively small. In fact, a nondispersing feature appears near the Dirac energy in an energy window of 15 meV, as can be observed in the high-resolution ARPES data (see SM note 9 [37]), which could originate from the extended resonance states. The coexistence of gap opening and gap filling owing to the magnetic dopants has been reported in V-doped Sb_2Te_3, where both full QAHE and a finite DOS near Dirac energy are observed [46]. On the other hand, the tunneling spectra provide microscopic evidence of the absence of a large mass gap as expected, suggesting a weak coupling between the magnetic order and the topological states. While it is hard to pin down whether or not the defects shrink the mass gap from our experiments, they induce striking resonance states that could fill the gap. It would be interesting to check the evolution of impurity scattering and magnetic interactions against the position of Dirac energy relative to the Fermi level in these compounds in the future. Finally, we note that the spin texture and the warping effects of the Dirac dispersion are still governed by the cubic spin-orbit coupling [41] far away from the Dirac energy, so that the CECs and QPI patterns can be well captured by the model with paramagnetic order.

In summary, we have studied the scattering properties and spatial structures of the topological states in the newly discovered Mn124 and Mn147. Our QPI measurements reveal the helical spin texture of the surface states, confirming their topological nature. The spatial evolution of the local DOS allows us to identify the extended resonance states associated with native defects in MBT SL, suggesting that the finite DOS near the Dirac energy may not be inconsistent with a small mobility gap opening. These findings have established Mn124 and 147 as excellent platforms to realize exotic quantum phenomena, in addition to being a path to obtain ideal samples for the realization of these phenomena at higher temperatures.

We thank Vidya Madhavan, Lin Jiao, Shichao Yan, Yue Zhao, and Jorge Olivares Rodriguez for helpful discussions. This work is supported by the National Key R&D Program of China (Grants No. 2016YFA0300201 and No. 2017YFA0303001), the Anhui Initiative in Quantum Information Technologies (Grant No. AHY160000), the Key Research Program of Frontier Sciences of the CAS (Grant No. QYZDY-SSW-SLH021), the National Natural Science Foundation of China (NNSFC, Grants No. 11534010 and No. 11888101) and Hefei Science Center of the CAS (Grant No. 2016HSC-IU001). Z.Y.W. acknowledges the USTC startup fund. Z.J.W. acknowledges support from the NNSFC (Grant No. 11974395), the Strategic Priority Research Program of CAS (Grant No. XDB33000000), and the CAS Pioneer Hundred Talents Program. G.X. is supported by the National Key R&D Program of China (No. 2018YFA0307000), and the NNSFC (No. 11874022).

[1] Y. Tokura, K. Yasuda, and A. Tsukazaki, Magnetic topological insulators, Nat. Rev. Phys. **1**, 126 (2019).

[2] R. Yu, W. Zhang, H. Zhang, S.-C. Zhang, X. Dai, and Z. Fang, Quantized anomalous Hall effect in magnetic topological insulators, Science **329**, 61 (2010).

[3] C.-Z. Chang, J. Zhang, X. Feng, J. Shen, Z. Zhang, M. Guo, K. Li, Y. Ou, P. Wei, L.-L. Wang, Z.-Q. Ji, Y. Feng, S. Ji, X. Chen, J. Jia, X. Dai, Z. Fang, S.-C. Zhang, K. He, Y. Wang *et al.*, Experimental observation of the quantum anomalous Hall effect in a magnetic topological insulator, Science **340**, 167 (2013).

[4] D. Xiao, J. Jiang, J.-H. Shin, W. Wang, F. Wang, Y.-F. Zhao, C. Liu, W. Wu, M. H. W. Chan, N. Samarth, and C.-Z. Chang, Realization of the Axion Insulator State in Quantum Anomalous Hall Sandwich Heterostructures, Phys. Rev. Lett. **120**, 056801 (2018).

[5] M. Mogi, M. Kawamura, R. Yoshimi, A. Tsukazaki, Y. Kozuka, N. Shirakawa, K. S. Takahashi, M. Kawasaki, and Y. Tokura, A magnetic heterostructure of topological insulators as a candidate for an axion insulator, Nat. Mater. **16**, 516 (2017).

[6] Q.-L. He, L. Pan, A. L. Stern, E. C. Burks, X. Che, G. Yin, J. Wang, B. Lian, Q. Zhou, E. S. Choi, K. Murata, X. Kou, Z. Chen, T. Nie, Q. Shao, Y. Fan, S.-C. Zhang, K. Liu, J. Xia, and K. L. Wang, Chiral Majorana fermion modes in a quantum anomalous Hall insulator–superconductor structure, Science **357**, 294 (2017).

[7] Q. Liu, C.-X. Liu, C. Xu, X.-L. Qi, and S.-C. Zhang, Magnetic Impurities on the Surface of a Topological Insulator, Phys. Rev. Lett. **102**, 156603 (2009).

[8] Y. L. Chen, J. G. Analytis, J.-H. Chu, Z. K. Liu, S.-K. Mo, X. L. Qi, H. J. Zhang, D. H. Lu, X. Dai, Z. Fang, S. C. Zhang, I. R. Fisher, Z. Hussain, and Z.-X. Shen, Experimental realization of a three-dimensional topological insulator Bi_2Te_3, Science **325**, 178 (2009).

[9] F. Katmis, V. Lauter, F. S. Nogueira, B. A. Assaf, M. E. Jamer, P. Wei, B. Satpati, J. W. Freeland, I. Eremin, D. Heiman, P. Jarillo-Herrero, and J. S. Moodera, A high-temperature ferromagnetic topological insulating phase by proximity coupling, Nature (London) **533**, 513 (2016).

[10] G. Xu, B. Lian, and S.-C. Zhang, Intrinsic Quantum Anomalous Hall Effect in the Kagome Lattice $Cs_2LiMn_3F_{12}$, Phys. Rev. Lett. **115**, 186802 (2015).

[11] J.-X. Yin, W. Ma, T. A. Cochran, X. Xu, S.-S. Zhang, H.-J. Tien, N. Shumiya, G. Cheng, K. Jiang, B. Lian, Z. Song, G. Chang, I. Belopolski, D. Multer, M. Litskevich, Z.-J. Cheng, X.-P. Yang, B. Swidler, H.-B. Zhou, H. Lin *et al.*, Quantum-limit Chern topological magnetism in $TbMn_6Sn_6$, Nature (London) **583**, 533 (2020).

[12] J.-H. Li, Y. Li, S.-Q. Du, Z. Wang, B.-L. Gu, S.-C. Zhang, K. He, W.-H. Duan, and Y. Xu, Intrinsic magnetic topological insulators in van der Waals layered $MnBi_2Te_4$-family materials, Sci. Adv. **5**, eaaw5685 (2019).

[13] J.-H. Cui, M.-Z. Shi, H.-H. Wang, F.-H. Yu, T. Wu, X.-G. Luo, J.-J. Ying, and X.-H. Chen, Transport properties of thin flakes of the antiferromagnetic topological insulator $MnBi_2Te_4$, Phys. Rev. B **99**, 155125 (2019).

[14] Y. Gong, J.-W. Guo, J.-H. Li, K.-J. Zhu, M.-H. Liao, X.-Z. Liu, Q.-H. Zhang, L. Gu, L. Tang, X. Feng, D. Zhang, W. Li, C.-L. Song, L.-L. Wang, P. Yu, X. Chen, Y.-Y. Wang, H. Yao, W.-H. Duan, Y. Xu *et al.*, Experimental realization of an intrinsic magnetic topological insulator, Chin. Phys. Lett. **36**, 076801 (2019).

[15] J.-Q. Yan, Q. Zhang, T. Heitmann, Z.-L. Huang, K.-Y. Chen, J.-G. Cheng, W.-D. Wu, D. Vaknin, B. C. Sales, and R. J. McQueeney, Crystal growth and magnetic structure of $MnBi_2Te_4$, Phys. Rev. Mater. **3**, 064202 (2019).

[16] A. Zeugner, F. Nietschke, A. U. B. Wolter, S. Gaß, R. C. Vidal, T. R. F. Peixoto, D. Pohl, C. Damm, A. Lubk, R. Hentrich, S. K. Moser, C. Fornari, C. H. Min, S. Schatz, K. Kißner, M. Ünzelmann, M. Kaiser, F. Scaravaggi, B. Rellinghaus, K. Nielsch *et al.*, Chemical aspects of the antiferromagnetic topological insulator $MnBi_2Te_4$, Chem. Mater. **31**, 2795 (2019).

[17] B. Chen, F.-C. Fei, D.-Q. Zhang, B. Zhang, W.-L. Liu, S. Zhang, P.-D. Wang, B.-Y. Wei, Y. Zhang, Z.-W. Zuo, J.-W. Guo, Q.-Q. Liu, Z.-L. Wang, X.-C. Wu, J.-Y. Zong, X.-D. Xie, W. Chen, Z. Sun, S.-C. Wang, Y. Zhang *et al.*, Intrinsic magnetic topological insulator phases in the Sb doped $MnBi_2Te_4$ bulks and thin flakes, Nat. Commun. **10**, 4469 (2019).

[18] S. H. Lee, Y.-L. Zhu, Y. Wang, L.-X. Miao, T. Pillsbury, H.-M. Yi, S. Kempinger, J. Hu, C. A. Heikes, P. Quarterman, W. Ratcliff, J. A. Borchers, H.-D. Zhang, X.-L. Ke, D. Graf, N. Alem, C.-Z. Chang, N. Samarth, and Z.-Q. Mao, Spin scattering and noncollinear spin structure-induced intrinsic anomalous Hall effect in antiferromagnetic topological insulator $MnBi_2Te_4$, Phys. Rev. Research **1**, 012011(R) (2019).

[19] C.-W. Hu, K. N. Gordon, P.-F. Liu, J.-Y. Liu, X.-Q. Zhou, P.-P. Hao, D. Narayan, E. Emmanouilidou, H.-Y. Sun, Y.-T. Liu, H. Brawer, A. P. Ramirez, L. Ding, H.-B. Cao, Q.-H. Liu, D. Dessau, and N. Ni, A van der Waals antiferromagnetic topological insulator with weak interlayer magnetic coupling, Nat. Commun. **11**, 97 (2020).

[20] J.-Z. Wu, F.-C. Liu, M. Sasase, K. Ienaga, Y. Obata, R. Yukawa, K. Horiba, H. Kumigashira, S. Okuma, T. Inoshita, and H. Hosono, Natural van der Waals heterostructural single crystals with both magnetic and topological properties, Sci. Adv. **5**, eaax9989 (2019).

[21] R. C. Vidal, A. Zeugner, J. I. Facio, R. Ray, M. H. Haghighi, A. U. B. Wolter, L. T. C. Bohorquez, F. Caglieris, S. Moser, T. Figgemeier, T. R. F. Peixoto, H. B. Vasili, M. Valvidares, S.-W. Jung, C. Cacho, A. Alfonsov, K. Mehlawat, V. Kataev, C. Hess, M. Richter *et al.*, Topological Electronic Structure and Intrinsic Magnetization in $MnBi_4Te_7$: A Bi_2Te_3 Derivative with a Periodic Mn Sublattice, Phys. Rev. X **9**, 041065 (2019).

[22] H.-Y. Sun, B.-W. Xia, Z.-J. Chen, Y.-J. Zhang, P.-F. Liu, Q.-S. Yao, H. Tang, Y.-J. Zhao, H. Xu, Q.-H. Liu, and R. Design, Principles of the Quantum Anomalous Hall Effect in Superlatticelike Magnetic Topological Insulators, Phys. Rev. Lett. **123**, 096401 (2019).

[23] Y.-J. Deng, Y.-J. Yu, M.-Z. Shi, Z.-X. Guo, Z.-H. Xu, J. Wang, X.-H. Chen, and Y.-B. Zhang, Quantum anomalous Hall effect in intrinsic magnetic topological insulator $MnBi_2Te_4$, Science **367**, 895 (2020).

[24] C. Liu, Y.-C. Wang, H. Li, Y. Wu, Y.-X. Li, J.-H. Li, K. He, Y. Xu, J.-S. Zhang, and Y.-Y. Wan, Robust axion insulator and Chern insulator phases in a two-dimensional antiferromagnetic topological insulator, Nat. Mater. **19**, 522 (2020).

[25] Y. J. Chen, L. X. Xu, J. H. Li, Y. W. Li, H. Y. Wang, C. F. Zhang, H. Li, Y. Wu, A. J. Liang, C. Chen, S. W. Jung, C. Cacho, Y. H. Mao, S. Liu, M. X. Wang, Y. F. Guo, Y. Xu, Z. K. Liu, L. X. Yang, and Y. L. Chen, Topological Electronic Structure and Its Temperature Evolution in Antiferromagnetic Topological Insulator $MnBi_2Te_4$, Phys. Rev. X **9**, 041040 (2019).

[26] H. Li, S.-Y. Gao, S.-F. Duan, Y.-F. Xu, K.-J. Zhu, S.-J. Tian, J.-C. Gao, W.-H. Fan, Z.-C. Rao, J.-R. Huang *et al.*, Dirac Surface States in Intrinsic Magnetic Topological Insulators $EuSn_2As_2$ and $MnBi_{2n}Te_{3n+1}$, Phys. Rev. X **9**, 041039 (2019).

[27] Y.-J. Hao, P.-F. Liu, Y. Feng, X.-M. Ma, E. F. Schwier, M. Arita, S. Kumar, C.-W. Hu, Rui'e Lu, M. Zeng, Y. Wang, Z.-Y. Hao, H.-Y. Sun, K. Zhang, J.-W. Mei, N. Ni, L.-S. Wu, K. Shimada, C.-Y. Chen, Q.-H. Liu, and C. Liu, Gapless Surface Dirac Cone in Antiferromagnetic Topological Insulator $MnBi_2Te_4$, Phys. Rev. X **9**, 041038 (2019).

[28] P. Swatek, Y. Wu, L.-L. Wang, K. Lee, B. Schrunk, J.-Q. Yan, and A. Kaminski, Gapless Dirac surface states in the antiferromagnetic topological insulator $MnBi_2Te_4$, Phys. Rev. B **101**, 161109(R) (2020).

[29] Y. Hu, L.-X. Xu, M.-Z. Shi, A.-Y. Luo, S.-T. Peng, Z.-Y. Wang, J.-J. Ying, T. Wu, Z.-K. Liu, C.-F. Zhang, Y.-L. Chen, G. Xu, X.-H. Chen, and J.-F. He, Universal gapless Dirac cone and tunable topological states in $(MnBi_2Te_4)_m(Bi_2Te_3)_n$ heterostructures, Phys. Rev. B **101**, 161113(R) (2020).

[30] M. M. Otrokov, I. I. Klimovskikh, H. Bentmann, D. Estyunin, A. Zeugner, Z. S. Aliev, S. Gaß, A. U. B. Wolter, A. V. Koroleva, A. M. Shikin, M. Blanco-Rey, M. Hoffmann, I. P. Rusinov, A. Yu. Vyazovskaya, S. V. Eremeev, Yu. M. Koroteev,

V. M. Kuznetsov, F. Freyse, J. Sánchez-Barriga *et al.*, Prediction and observation of an antiferromagnetic topological insulator, Nature (London) **576**, 416 (2019).

[31] E. D. L. Rienks, S. Wimmer, J. Sánchez-Barriga, O. Caha, P. S. Mandal, J. Růžička, A. Ney, H. Steiner, V. V. Volobuev, H. Groiss, M. Albu, G. Kothleitner, J. Michalička, S. A. Khan, J. Minár, H. Ebert, G. Bauer, F. Freyse, A. Varykhalov, O. Rader, and G. Springholz, Large magnetic map at the Dirac point in $Bi_2Te_3/MnBi_2Te_4$ heterostructures, Nature (London) **576**, 423 (2019).

[32] H. Beidenkopf, P. Roushan, J. Seo, L. Gorman, I. Drozdov, Y. S. Hor, R. J. Cava, and A. Yazdani, Spatial fluctuations of helical Dirac fermions on the surface of topological insulators, Nat. Phys. **7**, 939 (2011).

[33] Z. Alpichshev, R. R. Biswas, A. V. Balatsky, J. G. Analytis, J.-H. Chu, I. R. Fisher, and A. Kapitulnik, STM Imaging of Impurity Resonances on Bi_2Se_3, Phys. Rev. Lett. **108**, 206402 (2012).

[34] I. Lee, C. K. Kim, J. Lee, S. J. L. Billinge, R. Zhong, J. A. Schneeloch, T.-S. Liu, T. Valla, J. M. Tranquada, G. Gu, and J. C. Séamus Davis, Imaging Dirac-mass disorder from magnetic dopant atoms in the ferromagnetic topological insulator $Cr_x(Bi_{0.1}Sb_{0.9})_{2-x}Te_3$, Proc. Natl. Acad. Sci. USA **112**, 1316 (2015).

[35] R. R. Biswas and A. V. Balatsky, Impurity-induced states on the surface of three-dimensional topological insulators, Phys. Rev. B **81**, 233405 (2010).

[36] M.-Z. Shi, B. Lei, C.-S. Zhu, D.-H. Ma, J.-H. Cui, Z.-L. Sun, J.-J. Ying, and X.-H. Chen, Magnetic and transport properties in the magnetic topological insulators $MnBi_2Te_4(Bi_2Te_3)_n (n = 1, 2)$, Phys. Rev. B **100**, 155144 (2019).

[37] See Supplemental Material at http://link.aps.org/supplemental/10.1103/PhysRevB.102.161115 for more topographic images, tunneling spectra, QPI analysis and calculations.

[38] Y.-P. Jiang, Y. Y. Sun, M. Chen, Y.-L. Wang, Z. Li, C.-L. Song, K. He, L. L. Wang, X. Chen, Q.-K. Xue, X.-C. Ma, and S.-B. Zhang, Fermi-Level Tuning of Epitaxial Sb_2Te_3 Thin Films on Graphene by Regulating Intrinsic Defects and Substrate Transfer Doping, Phys. Rev. Lett. **108**, 066809 (2012).

[39] R. Feenstra, J. Stroscio, and A. Fein, Tunneling spectroscopy of the Si (111) $2\times$ 1 surface, Surf. Sci. **181**, 295 (1987).

[40] M. P. Allan, F. Massee, D. K. Morr, J. Van Dyke, A. W. Rost, A. P. Mackenzie, C. Petrovic, and J. C. Davis, Imaging Cooper pairing of heavy fermions in $CeCoIn_5$, Nat. Phys. **9**, 468 (2013).

[41] L. Fu, Hexagonal Warping Effects in the Surface States of the Topological Insulator Bi_2Te_3, Phys. Rev. Lett. **103**, 266801 (2009).

[42] J. Wang, W. Li, P. Cheng, C.-L. Song, T. Zhang, P. Deng, X. Chen, X.-C. Ma, K. He, J.-F. Jia, Q.-K. Xue, and B.-F. Zhu, Power-law decay of standing waves on the surface of topological insulators, Phys. Rev. B **84**, 235447 (2011).

[43] D. Nevola, H.-X. Li, J.-Q. Yan, R. G. Moore, H.-N. Lee, H. Miao, and P. D. Johnson, Coexistence of Surface Ferromagnetism and a Gapless Topological State in $MnBi_2Te_4$, Phys. Rev. Lett. **125**, 117205 (2020).

[44] X.-F. Wu, J.-Y. Li, X.-M. Ma, Y. Zhang, Y.-T. Liu, C.-S. Zhou, J.-F. Shao, Q.-M. Wang, Y.-J. Hao, Y. Feng, E. F. Schwier, S. Kumar, H.-Y. Sun, P.-F. Liu, K.-Y. Shimada, K. Miyamoto, T. Okuda, K.-D. Wang, M.-H. Xie, C.-Y. Chen, Q.-H. Liu, C. Liu, and Y. Zhao, Distinct Topological Surface States on the Two Terminations of $MnBi_4Te_7$, Phys. Rev. X **10**, 031013 (2020).

[45] P. M. Sass, J. Kim, D. Vanderbilt, J.-Q. Yan, and W.-A. Wu, Robust A-Type Order and Spin-Flop Transition on the Surface of the Antiferromagnetic Topological Insulator $MnBi_2Te_4$, Phys. Rev. Lett. **125**, 037201 (2020).

[46] P. Sessi, R. R. Biswas, T. Bathon, O. Storz, S. Wilfert, A. Barla, K. A. Kokh, O. E. Tereshchenko, K. Fauth, M. Bode, and A. V. Balatsky, Dual nature of magnetic dopants and competing trends in topological insulators, Nat. Commun. **7**, 12027 (2016).